Differential Rotation and Cloud Texture: Analysis Using Generalized Scale Invariance

K. PFLUG AND S. LOVEJOY

Department of Physics, McGill University, Montreal, Quebec, Canada

D. SCHERTZER

Laboratoire de Météorologie Dynamique, Université Pierre et Marie Curie, Paris, France

(Manuscript received 30 August 1991, in final form 20 April 1992)

ABSTRACT

The standard picture of atmospheric dynamics is that of an isotropic two-dimensional large scale and an isotropic three-dimensional small scale, the two separated by a dimensional transition called the "mesoscale gap." Evidence now suggests that, on the contrary, atmospheric fields, while strongly anisotropic, are nonetheless scale invariant right through the mesoscale. Using visible and infrared satellite cloud images and the formalism of generalized scale invariance (GSI), the authors attempt to quantify the anisotropy for cloud radiance fields in the range 1–1000 km. To do this, the statistical translational invariance of the fields is exploited by studying the anisotropic scaling of lines of constant Fourier amplitude.This allows the investigation of the change in shape and orientation of average structures with scale.

For the three texturally—and meteorologically—very different images analyzed, three different generators of anisotropy are found that generally reproduce well the Fourier space anisotropy. Although three cases are a small number from which to infer ensemble-averaged properties, the authors conclude that while cloud radiances are not isotropic (self-similar), they are nonetheless scaling. Since elsewhere (with the help of simulations) it is shown that the generator of the anisotropy is related to the texture, it is argued here that GSI could potentially provide a quantitative basis for cloud classification and modeling.

1. Introduction

In the standard picture of atmospheric dynamics, the atmosphere consists of two isotropic regimes—a two-dimensional large-scale turbulence and a three-dimensional small-scale turbulence—separated by a "mesoscale gap" (Monin 1972; Van der Hoven 1957). According to this view, the two isotropic regimes should be dynamically quite different (for a review, see Lesieur 1987). This is because of the conservation of vorticity in two but not three dimensions, hence the existence—for the velocity field—of two quadratic invariants (enstrophy and energy fluxes) in two dimensions, but only one in three dimensions (the energy flux). This different physics leads to different spectral power laws for the corresponding velocity fields (Kraichnan 1967). If the two regimes were to coexist, then they ought to be separated by a drastic *dimensional transition* (Schertzer and Lovejoy 1985a). For associated fields for which only one conserved quantity exists in either two or three dimensions, this will be quite abrupt. In the case of passive scalars, it leads to algebraic behavior in three dimensions but to exponential behavior in two (Larchevesque and Lesieur 1981). On the contrary, there is now considerable experimental evidence indicating that the (power law) energy spectra of horizontal fluctuations of the horizontal wind continue through the mesoscale unchanged for scales ranging from about 1 mm to at least several hundred kilometers in the horizontal. In a recent paper (Lovejoy et al. 1992b), a systematic spectral analysis of a large number of satellite pictures (GOES, NOAA, and Landsat satellites were used over visible, thermal infrared, and near-infrared wavelengths) spanning the range 160 m to 4000 km (the entire mesoscale) confirms the scaling down to at least 300 m. For reviews see Lilly (1983) and Schertzer and Lovejoy (1985a), and for evidence, see Pinus (1968), Vinnichenko (1970), Brown and Robinson (1979), Gage (1979), Atkinson (1981), Balsley and Carter (1982), Van Zandt (1982), and Nastrom and Gage (1983). In the vertical, in spite of the exponential falloff in the mean pressure, the fluctuations in the horizontal wind also seem to be scaling (Endlich et al. 1969; Adelfang 1971; Schertzer and Lovejoy 1985a) from scales for shears over layers as thin as 100 m to about 15–18 km thick. In addition, several scaling analyses of the more readily accessible radar rain reflectivities and cloud radiance data have recently been published (Lovejoy 1982; Rhys and Waldvogel 1986; Lovejoy et al. 1987; Gabriel et al. 1988; Welch et al. 1988; Cahalan and Joseph 1989; Detwiller 1990; Lovejoy and Schertzer 1990a, 1991; Cahalan 1991; Yano and Takeuchi 1991; Tessier et al. 1992) suggesting that scale invariance is indeed a basic symmetry of the atmosphere. [See Lovejoy and Schertzer (1990a), appendix A, for a discussion of the limitations and problems of using (early) monofractal analysis

---

Corresponding author address: Dr. Shaun Lovejoy, Department of Physics, McGill University, Ernest Rutherford Physics Bldg., 3600 University St., Montreal, H3A 2T8 Quebec, Canada.

techniques on multifractal data. The use of inappropriate analysis techniques is one source of claims of breaks in the scaling.]

Based on these observations a new *unified scaling* model of atmospheric turbulence has been proposed as a simpler alternative to the standard model (Schertzer and Lovejoy 1983, 1985a,b, 1989a,b; Lovejoy and Schertzer 1985, 1986; Lovejoy et al. 1992b). In contrast to the 2D/3D dichotomy, this model is based on generalized scale invariance (GSI) and posits scale invariance as the fundamental assumption. Isotropy is not required nor expected; hence, there is no need for separate dynamical regimes at small and large scales. Instead, one anisotropic, scale-invariant regime covers most of the meteorologically significant range of scales. Rather than distinct large- and small-scale isotropic cascades, the dynamics are ruled by nonlinearly coupled anisotropic cascades with no mesoscale break. Theoretically, this unified scaling model is justified because, over the corresponding ranges, the equations governing the dynamics have no characteristic length; hence, they admit scaling solutions (e.g., see Schertzer and Lovejoy 1987b). This also appears to be true of many of the relevant boundary conditions, such as surface topography (e.g., Venig-Meinesz 1951; Bills and Kobrick 1985; Lovejoy and Schertzer 1990c; Lavallée et al. 1992).

The aim of the research described in this paper is to develop some analysis techniques for studying GSI in satellite cloud images and then, using these techniques, try to quantify the observed anisotropy. Since the full nonlinear GSI is so general (see examples in Schertzer and Lovejoy 1985b, 1988, 1991), it would be extremely difficult to investigate all possibilities without studying the symmetries restricting the Lie algebra of the anisotropy generator (Schertzer and Lovejoy 1991). A study of such "Lie cascades" will be developed elsewhere. To make the problem more easily tractable, we focus on the linear approximation (e.g., the generators of the anisotropy **G** are matrices), basing our analysis techniques on this approximation. Linear approximations to nonlinear GSI will always be valid over small enough ranges of scale, and the full nonlinear generator may be inferred from a series of linearizations (tangent planes).

To investigate linear GSI in the atmosphere, satellite cloud images are analyzed to determine parameters of the linear generalized scaling transformations under which the radiance field is scaling. To do this, contours of the amplitude in Fourier space are used to separate the structures with different scales. By analyzing satellite images with the new "Monte Carlo differential rotation" technique, linear GSI is studied in the two horizontal dimensions. This enables us, for the first time, to study the rotation produced by the Coriolis force in a scaling framework.

The research described here is the outcome of work undertaken for a master's thesis and is described more fully in Pflug (1991). [Preliminary results are reported in Pflug et al. (1991) and a brief summary in Lovejoy et al. (1992a).]

2. Generalized scale invariance

a. Discussion

Scale invariance is a symmetry respected by systems whose large- and small-scale features statistically resemble each other in some way. For such systems, there exists a transformation, which is a function only of the scale ratio, that relates the physical properties (structures) at different scales through power-law relations (we will ignore any log corrections). In isotropic systems, the relevant scale-changing transformation is an isotropic magnification by a scale ratio (λ). Systems invariant under such isotropic transformations are self-similar and inhomogeneous sets that possess this symmetry are self-similar fractals.

It is now known, however, that in scaling fields (more precisely, in scaling mathematical measures in contrast to scaling geometric sets) we generally obtain multiple rather than "mono" scaling; they are multifractals (Grassberger 1983; Hentschel and Procaccia 1983; Schertzer and Lovejoy 1983, 1984, 1987a,b, 1989a, 1991, 1992; Parisi and Frisch 1985; Halsey et al. 1986). In contrast to monoscaling, in multiple scaling different statistical moments (different powers of the field) have different scaling exponents. Such fields also have infinitely many fractal dimensions,[1] each of which describes the distribution of regions of a different intensity. In this work, however, the multifractal nature of the atmospheric radiance field (Gabriel et al. 1988; Lovejoy and Schertzer 1990d; Tessier et al. 1993) is not considered;[2] we focus instead on the anisotropy and only study a second-order moment, the energy spectrum.

For concreteness, consider the structure function $S(\mathbf{x})$ of the field $f(\mathbf{x})$:

$$S(\mathbf{x}) = \langle (f(\mathbf{x}') - f(\mathbf{x} + \mathbf{x}'))^2 \rangle \qquad (1a)$$

where $\langle \quad \rangle$ means statistical or ensemble averaging. We will now assume statistical translational invariance of $f(\mathbf{x})$; this implies $S(\mathbf{x})$ is independent of $\mathbf{x}'$ as indicated. This is appropriate for the cloud radiances examined here since the fundamental physics of the cloud processes are likely to be independent of position. We therefore obtain:

$$S(\mathbf{x}) = 2(\langle f(\mathbf{x}')^2 \rangle - \langle f(\mathbf{x}') f(\mathbf{x}) \rangle) \qquad (1b)$$

$$S(\mathbf{x}) = 2(\langle f(0)^2 \rangle - \langle f(0) f(\mathbf{x}) \rangle). \qquad (1c)$$

---

[1] It has recently been shown (Schertzer and Lovejoy 1987a, 1989, 1991) that multifractals have stable, attractive universality classes depending on only three exponents, which considerably simplify their analysis and simulation.

[2] The last two papers not only test the multifractal nature of the radiances, they also estimate the universal exponents, which were found to be very close to those of the velocity field (Schmitt et al. 1992).

If the field is scale invariant, the structure function has the following additional property:

$$S(\mathbf{T}_\lambda \mathbf{x}) = \lambda^{-2H} S(\mathbf{x}) \qquad (2)$$

where $\mathbf{T}_\lambda$ is the scale reduction operator that reduces the scale of the vector $\mathbf{x}$ by the factor λ (in self-similar, isotropic scale invariance, $\mathbf{T}_\lambda = \lambda^{-1}\mathbf{I}$ where $\mathbf{I}$ is the identity operator), λ is a scale ratio, and H is the scaling exponent of the second moment.

Since all real systems possess finite inner and outer scales, the relationship expressed by Eq. (2) will hold only within these limits. The region between these limits is the scale-invariant regime. The extent of the scale-invariant regime for the atmospheric velocity field was discussed briefly in the Introduction. The inner limit for the radiation fields is still not known (and is likely to vary from one realization/synoptic situation to another). It seems likely that it is typically quite small since radiances are not obviously uniform even at scales as small as a meter.

b. The elements of generalized scale invariance

In order to go beyond isotropic scale invariance, it is necessary to generalize the notion of scale and scale change such that anisotropic systems satisfy Eq. (2) but with $\mathbf{T}_\lambda$ no longer an isotropic reduction. This general definition consists of the following three ingredients (Schertzer and Lovejoy 1985b, 1987b, 1988):

1) an initial "ball," B_1, defining the unit scale ($\lambda = 1$), from which all other scales are generated;
2) a generator, $\mathbf{G}$, which defines the one parameter (semi) group of scale transformations, $\mathbf{T}_\lambda = \lambda^{-\mathbf{G}}$. In the isotropic case, the generator is the identity and a scale change is simply $\lambda^{-1}\mathbf{I}$.
3) some measure of scale, φ.

In generalized scale invariance, the information that defines the nature of scale changes (the anisotropy) is contained in the generator $\mathbf{G}$, the trace of which (denoted Tr$\mathbf{G}$) defines the overall contraction of space with scale changes and is called the *elliptical dimension* d_{el}. When structures are differentially stratified (e.g., by the action of gravity), d_{el} is reduced from its isotropic value [(=3 in (x, y, z) space], and quantifies the degree of stratification. For example, based on theoretical arguments and empirical analyses, Schertzer and Lovejoy (1985a) estimated that d_{el} for the horizontal wind was $23/9 \approx 2.555 \cdots$ which falls between the completely stratified value 2 and the isotropic value 3. Similarly, using "elliptical dimensional sampling," Lovejoy et al. (1987) empirically estimated that d_{el} for radar reflectivities from rain was 2.22 ± 0.07.

In the isotropic case in dimension D, the measure of scale, φ, is conveniently taken as the $1/D$ power of the D-dimensional volume and satisfies $\varphi(B_1) = 1$ and $\varphi(B_\lambda) = \lambda^{-1}$. In general, the anisotropic measure of scale, φ_{el} ("el" signifies "elliptical" for anisotropy), satisfies $\varphi_{\text{el}}^{d_{\text{el}}}(B_\lambda) = \varphi^D(B_\lambda) = \varphi_{\text{el}}^{d_{\text{el}}}(\mathbf{T}_\lambda B_1) = \lambda^{-d_{\text{el}}}\varphi_{\text{el}}^{d_{\text{el}}}(B_1)$, where d_{el} is the elliptical dimension mentioned above, that is, $\varphi_{\text{el}}(B_\lambda) = \lambda^{-1}$. The definition of φ_{el} is, to some extent, arbitrary. Any positive power of the chosen definition would be suitable since $\mathbf{G}$ would only change by an overall constant factor to compensate.

In order that the definition of scale be unambiguous, we must impose a restriction on $\mathbf{G}$ so the balls are strictly decreasing with λ; whenever $\lambda_2 > \lambda_1$ the set $B_{\lambda 2}$ must be completely contained within the set $B_{\lambda 1}$. This is necessary so that each vector can be uniquely associated with a given scale ratio. In general, if the real parts of the (generalized) eigenvalues of $\mathbf{G}$ are positive (Schertzer and Lovejoy 1985b), then it is possible to choose some B_1 so that a GSI system may be defined. However, it is often convenient to use an isotropic unit ball—a spheroscale (Schertzer and Lovejoy 1983)—which leads to the more restrictive condition that the eigenvalues of the symmetric part of $\mathbf{G}$ be positive. The existence of a spheroscale, however, is a simplifying assumption that depends on the existence of at least one scale at which all directions are equivalent, and is not necessary. Although this assumption may seem reasonable for horizontal sections in the atmosphere, it is empirically confirmed for only two of the cases analyzed here, and in general, we will see that the assumption must be dropped.

Because the scale-changing operators depend only on the scale ratio, they form a semigroup and take the form:

$$\mathbf{T}_\lambda = \lambda^{-\mathbf{G}}. \qquad (3)$$

When the generator $\mathbf{G}$ is linear (a matrix), we may interpret the exponentiation by the series expansion of $\exp(-\mathbf{G}\log\lambda)$. When $\mathbf{G}$ is nonlinear, however, we may consider it as defining a local infinitesimal scale change. This is exactly analogous to the use of locally flat space–time in general relativity. [Indeed, astrophysicists have recently started to incorporate anisotropic scaling ideas into formulations of relativity (Carter and Henrickson 1992), and Schertzer and Lovejoy (1989b) have used GSI to model barred and spiral galaxies.] Introducing $u = \log\lambda$, we find:

$$\mathbf{T}du = \mathbf{I} - du\mathbf{G}, \quad \mathbf{I} = d\mathbf{T}_0. \qquad (4)$$

For specific nonlinear $\mathbf{G}$, this relation may be integrated (in general, numerically) to yield the finite scale changing operator $\mathbf{T}_u$.

We do not anticipate that linear GSI is better than a local approximation in the atmosphere, if only because the Coriolis force depends on latitude. For examples of nonlinear (and random) GSI, see Schertzer and Lovejoy (1985b, 1989a, 1991). The exact range of scales over which this approximation is valid in the atmosphere is not yet known, although it seems to be fairly good in the cases examined here, which cover ranges of scale of factors of about 500. However, even linear GSI allows for quite rich textures and structures as shown by the fractal cloud simulations in Lovejoy and Schertzer (1985, 1986). A matrix **G** contains textural information and can quantify simulated cloud textures and types. If the atmosphere respects GSI, then we expect that cloud texture is an anisotropic scale-invariant phenomenon that can be properly defined by a technique based on these fundamental characteristics. [A somewhat similar idea with respect to self-similar images was used by Pentland (1984) for image classification.] Even when considering linear GSI, the analysis is complicated by the statistical nature of the symmetry, that is, it is not respected exactly by individual images, only by ensemble averages. Furthermore, because this symmetry relates properties at different scales, large images with a wide range of represented scales are necessary to properly estimate **G**.

c. Linear GSI in two dimensions with a spheroscale

The images analyzed here are two-dimensional. With the simplifying assumptions that **G** is a position-independent matrix (linear GSI), and the unit scale is a spheroscale,[3] the contours defining various scales will be ellipses.

In linear GSI in two dimensions, **G** can be represented as a linear combination of four independent 2 × 2 matrices (quaternions) (Lovejoy and Schertzer 1985; Schertzer and Lovejoy 1985b) with the result that

$$\mathbf{G} = \begin{pmatrix} d+c & f-e \\ f+e & d-c \end{pmatrix} \qquad (5)$$

and, from Eq. (3):

$$\mathbf{T}_\lambda = \lambda^{-d}(\mathbf{I}\cosh(au) - (\mathbf{G} - \mathbf{I}d)\sinh(au)/a)$$

$$= \lambda^{-d}\begin{pmatrix} \cosh(au) - \frac{c}{a}\sinh(au) & -\frac{f-e}{a}\sinh(au) \\ -\frac{f+e}{a}\sinh(au) & \cosh(au) + \frac{c}{a}\sinh(au) \end{pmatrix} \qquad (6)$$

where c, d, f, and e are four real parameters and

$$a^2 = c^2 + f^2 - e^2. \qquad (7)$$

In this representation, the "elliptical dimension" is

$$d_{\mathrm{el}} = \mathrm{Tr}\mathbf{G} = 2d; \quad d_{\mathrm{el}} > 0 \quad \text{implies} \quad d > 0$$

and the condition on the eigenvalues of the symmetric part of **G** (which ensures that scales are uniquely defined; see above) implies

$$d^2 > c^2 + f^2. \qquad (8)$$

When the operator in Eq. (6) is applied to a circle at $\lambda = 1$ (a spheroscale), it yields a series of concentric ellipses. If the off-diagonal elements are nonzero, the ellipses rotate relative to one another. The values of the parameters c, e, and f determine how elliptical the contours may get and how much they rotate. In particular, two broad classes of behavior can be distinguished by the sign of the parameter a^2 (Schertzer and Lovejoy 1985b; Lovejoy and Schertzer 1985). The properties of scale changes within each of these classes can be determined by referring to the equations for the ellipticity ($\epsilon = B/A - 1$, where B/A is the axis ratio of elliptical contours) and angle of orientation (θ) of elliptical contours, which are developed in appendix A.

In the first case, $a^2 > 0$, a is real and the amount of rotation is limited. Only one spheroscale is encountered over the entire range of scales ($u = -\infty$ to ∞), since there is only one zero of Eqs. (24) and (25). The maximum amount of rotation possible is

$$|\Delta\theta|_{\max} = \theta(\infty) - \theta(-\infty) = \tan^{-1}(e/a). \qquad (9)$$

Note that since the major and minor axes switch at the spheroscale, the total *apparent* rotation will be $\pi/2$ greater. Unlike the rotation, however, the ellipticity is unlimited when $a^2 > 0$. This is the stratification-dominated case.

For the case $a^2 < 0$, a is imaginary, the amount of rotation is unlimited (rotation dominates), and there are infinitely many spheroscales[4] located between $u = -\infty$ and $u = \infty$. The ellipticity, however, is limited and the maximum ellipse axis ratio is

$$\left(\frac{B}{A}\right)_{\max} = 2\left(\frac{e}{|a|}\right)^2\left\{1 + \left[1 - \left(\frac{|a|}{e}\right)^2\right]^{1/2}\right\} - 1, \qquad (10)$$

where A and B are the ratios of the ellipse semiaxes to the spheroscale radius.

In both of the above cases, the scale ratio is defined to be

$$\lambda = (AB)^{1/2}. \qquad (11)$$

d. GSI in Fourier space

In this paper, the investigation of GSI is carried out in Fourier space. Fourier space operators that corre-

---

[3] Although the existence of a spheroscale appears to be an overly restrictive assumption, spheroscales were observed in most of the images examined throughout the course of this research (see Pflug 1991 for more examples). Thus, it is worthwhile to examine this case in detail.

[4] Equations (27) and (28) have infinitely many zeros; see appendix A for more details.

spond to the real space scaling operators are determined by analyzing contours of constant $\log\langle|F(\mathbf{k})|^2\rangle$, where $F(\mathbf{k})$ is the Fourier transform of the radiance field and $\mathbf{k}$ is the wavenumber. The reason for working in Fourier space is that for the images studied here, clouds are approximately statistically translationally invariant, which amounts to random phases in Fourier space. Since we are not interested in the location of structures in real space, only in their average aspect ratios and orientations as functions of scale, we need only consider the amplitude, $|F(\mathbf{k})|$, in Fourier space.

To obtain the Fourier space analog to the real space-scaling operator, we define $\tilde{\mathbf{T}}_\lambda = \lambda^{\mathbf{G}}$ to be the Fourier space-scaling operator defined by the requirement of invariance of the scalar product $(\mathbf{k}\cdot\mathbf{x})$ under scale changes (see appendix B for details). We thus obtain the following result:

$$\tilde{\mathbf{G}} = \mathbf{G}^T = \begin{pmatrix} d+c & f+e \\ f-e & d-c \end{pmatrix}. \qquad (12)$$

Assuming that the structure function satisfies Eq. (2), we obtain the Fourier space analog (appendix B):

$$P(\tilde{\mathbf{T}}_\lambda\mathbf{k}) = \lambda^{-(2H+d_{el})}P(\mathbf{k}), \qquad (13)$$

or

$$P_\lambda = \lambda^{-s}P_1, \qquad (14)$$

where $P(\mathbf{k}) = \langle|F(\mathbf{k})|^2\rangle$, $s = 2H + d_{el}$, $P_\lambda = P(\tilde{\mathbf{T}}_\lambda\mathbf{k}_1)$ ($\mathbf{k}_1$ is on the unit ball E_1) and $P_1 = P(\mathbf{k}_1)$. Taking the natural logarithm of Eq. (14), we obtain:

$$\log P_\lambda = -s\log\lambda + \log P_1. \qquad (15)$$

Typically, atmospheric energy spectra are defined within an isotropic framework, that is, with $\tilde{\mathbf{T}}_\lambda = \lambda\mathbf{I}$. The usual method involves integrating $P(\mathbf{k})$ over angles in Fourier space to obtain the energy $E(k)$, $k = |\mathbf{k}|$. The usual spectral exponent is denoted as β. These quantities are related to those used in this paper [$P(\mathbf{k})$ and s] as follows (dropping any constant integration factors):

$$E(k) \propto k^{D-1}P(k) \propto k^{-\beta}, \qquad (16)$$

where D is the dimension of space ($D = d_{el}$). Since $P(k) \propto k^{-s}$ in the isotropic case [Eq. (14)], we have

$$s = \beta - 1 + D, \qquad (17)$$

and, using $s = 2H + d_{el}$ (see above):

$$s = 2H + D; \quad \beta = 2H + 1. \qquad (18)$$

From Eqs. (14) and (18) and the definitions of s and β, we can define the anisotropic analog to $E(k)$ by integrating P_λ over generalized contours in Fourier space:

$$E_\lambda \propto \lambda^{d_{el}-1}P_\lambda. \qquad (19)$$

Finally, it should be emphasized that, although Eq. (14) applies to ensemble averages, we study single images in this paper. Since the $|F(\mathbf{k})|^2$ values for a single image will contain (occasionally large) fluctuations about the ensemble mean, individual images will not satisfy Eq. (14) exactly. Even so, we will still be able to obtain reasonable estimates of the parameters defining the anisotropy.

3. Data analysis

a. The Monte Carlo differential rotation technique

Quantifying the anisotropy in satellite cloud images using GSI amounts to estimating the parameters of both the unit ball and the generator. To do so, we use an approximate least-squares method, called the "Monte Carlo differential rotation" technique. The basic idea behind this technique is to fit the scaling parameters (s, P_1) and the generator parameters (c, e, and f; due to our definition of λ—our choice of φ—we have $d = 1$), as well as the various parameters needed to define the unit ball. To define the latter, it is convenient to parameterize the unit vectors by their polar coordinate equation: $\mathbf{k}_1 = [k_1(\theta), \theta)]$. Since the Fourier radius $k_1(\theta)$ is periodic in the polar angle θ, it is natural to parameterize it using the first few terms in a Fourier series. Since the field $f(\mathbf{x})$ is real, $P(\mathbf{k})$ must respect the symmetry $P(\mathbf{k}) = P(-\mathbf{k})$, hence, we must have $k_1(\theta) = k_1(\pi + \theta)$. We need therefore only consider an expansion in even multiples of θ. In all the cases examined, it was found that the following truncation was adequate:

$$k_1(\theta) = r_0 + a_1\cos2\theta + b_1\sin2\theta + a_2\cos4\theta + b_2\sin4\theta. \qquad (20)$$

In principle, any isoline of $P(\mathbf{k})$ could be used to define a unit scale. However, as will be seen below, in many cases visual inspection shows that roughly circular isolines exist. In these cases, the a, b parameters were set to zero and the best fit r_0 for a spheroscale was estimated. [Pflug (1991) visually examines the Fourier spaces of six other images; most of these show plausible spheroscales.]

Once the unit ball has been parameterized, the remaining parameters were estimated by minimizing the following approximate error function:

$$E_a^2 = \frac{1}{m}\sum_{i=1}^{m}(P_1 - \lambda(\mathbf{k}_i, \tilde{\mathbf{G}})^s P_\lambda(\mathbf{k}_i))^2, \qquad (21)$$

where the sum is over m randomly chosen Fourier pixels $\mathbf{k}_i$. Equation (21) is based on a rearrangement of Eq. (14) (i.e., $P_1 - \lambda^s P_\lambda = 0$). [An error function based on Eq. (15) (i.e., using $\log P$) was tested on one of the images analyzed and it was found that Eq. (21) produced slightly better results (see Pflug 1991 for details).] The error function is approximated by Monte Carlo techniques (the random selection of points) since an exact calculation (involving summing over each of the $N \times N$ Fourier pixels) would require solving the

FIG. 1. Image 1 (see text for description).

following transcendental equation $N \times N$ times to determine $\lambda(\mathbf{k}_i, \tilde{\mathbf{G}})$:

$$\mathbf{k}_1 = \tilde{\mathbf{T}}_\lambda^{-1}\mathbf{k}_\lambda \tag{22}$$

(i.e., for a given Fourier pixel $\mathbf{k}_i$, one must deduce the ratio λ^{-1} necessary to map the vector onto the unit ball). Since it is much simpler to calculate $\mathbf{k}_\lambda = \mathbf{k}(\lambda, \tilde{\mathbf{G}}, \mathbf{k}_1) = \tilde{\mathbf{T}}_\lambda \mathbf{k}_1$, (i.e., to calculate $\mathbf{k}_\lambda$ given $\mathbf{G}$ and $\mathbf{k}_1$), we choose instead to approximate the error function. This is done by selecting λ and θ randomly (see appendix C). We then calculate $\mathbf{k}_\lambda = \tilde{\mathbf{T}}_\lambda \mathbf{k}_1$ and determine $P(\mathbf{k}_\lambda)$ from the data. [Strictly speaking, we determine $|F(\mathbf{k})|^2$ from the data since $P(\mathbf{k})$ is an ensemble-average quantity and we are working with single images.] In Eq. (21) all of the parameters to be estimated enter through the calculation of $\mathbf{k}_\lambda$ (except P_1 which enters explicitly). The number of points in the subset is chosen so that the fluctuations in E_a due to the random selection of points in the sum are small relative to the variations in E_a with changes in the parameters. (For an image of size 256 × 256 pixels, typically 10 000 to 50 000 points are required, while, for an image of size 512 × 512 pixels, about 100 000 points are typically required.) Equation (21) is minimized by searching through a five- or six-dimensional parameter space (s, P_1, c, e, f, and perhaps r_0), varying each parameter successively, until a minimum is found. This minimization is then repeated to refine the parameter estimates and to ensure that the minima have not shifted significantly as each successive parameter is fit.[5] The parameter values and their errors are computed by fitting quadratics to E_a close to the minima.

Even with these shortcuts, the method can still be time consuming, involving many calculations of the "error" unless at least some of the parameters can be estimated or constrained beforehand. In practice, this can be done for at least some of the parameters. The spectral slope and intercept (s and P_1) can be approximated by computing the usual isotropic energy spectrum of an image [integrating $P(\mathbf{k})$ around circular annuli]. To obtain s and P_1 from β and E_1 (the corresponding isotropic parameters), we use $s = \beta + 1$ [Eq. (17) with $D = 2$] and $P_1 = E_1/2\pi$ [2π comes from the angular integration factor in Fourier space that was ignored in Eq. (16)]; c and f, on the other hand, are constrained by Eq. (8) to lie between -1 and 1 (since $d = 1$). However, the parameter e is not constrained (from Eqs. (7) and (8) $d^2 > a^2 + e^2$ but a^2 may be negative) and there is no obvious way of estimating it beforehand. The best way we found to locate its value is to begin searching within a large but reasonable range about $e = 0$ (say, $-5 \leqslant e \leqslant 5$), initially taking coarse steps to reduce the computation time.

b. Results

Image 1: Image 1 was the first image analyzed with the Monte Carlo differential rotation technique. This image is a 256 × 256 pixel *NOAA-9* Advanced Very High-Resolution Radiometer (AVHRR) IR image east of Labrador, Canada, with a resolution of about 1.1 km at nadir. (For convenience, in this analysis, distances will usually be measured in pixels, wavenumbers

FIG. 2. Smoothed Fourier transform of image 1. Smoothing emphasizes the Fourier space contours but was not used for the "Monte Carlo differential rotation" analysis.

---

[5] This method will work as long as the minimum is quite pronounced and there is no problem with multiple local minima. Due to our Monte Carlo estimates of the error, most standard minimization methods will not work: they require estimates of local derivatives in parameter space.

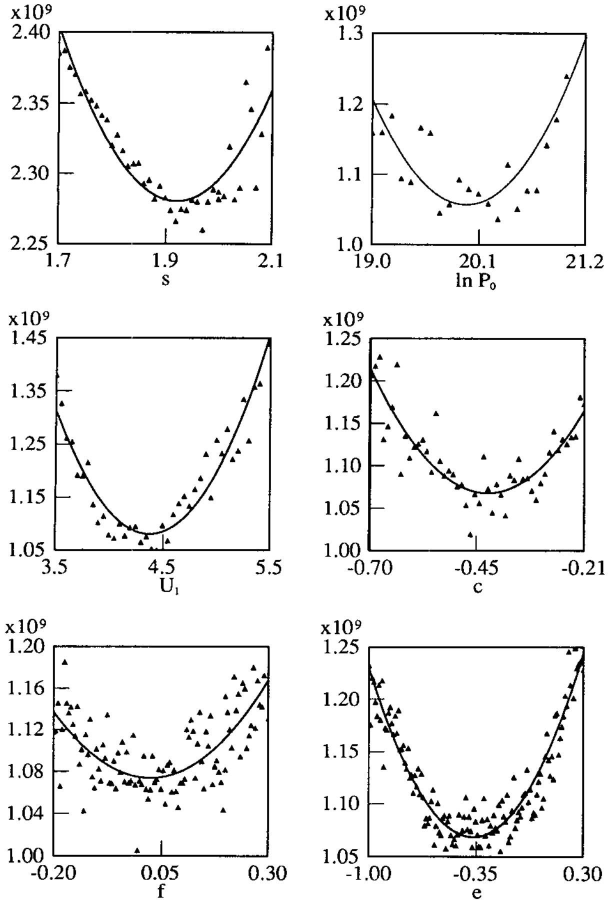

FIG. 3. E_a as a function of the parameters s, $\log P_0 = s \log r_0 + \log P_l$, $U_l = \log r_0$, c, f, and e for image 1. The symbols are data points and the solid lines are the fitted quadratics (note: $\log P_0 = s \log r_0 + \log P_l$).

TABLE 1. Results from the "Monte Carlo differential rotation" analysis. When a spheroscale exists (images 1, 2), r_0 is its scale in units of Fourier space pixels. To obtain the spheroscale in km, $1/r_0$ (km) $= N\Delta/r_0$ (pixels) was used, where N is the image dimension (in pixels) and Δ is the image resolution (in km). For image 3 s and $\log P_l$ were estimated from the isotropic spectrum.

	Image 1	Image 2	Image 3
s	1.92 ± .06	1.41 ± .04	2.10 ± .01
$\log P_l$	11.6 ± .6	18.8 ± .3	18.02 ± .08
$\log r_0$	4.4 ± .2	5.0 ± .2	no spheroscale
$\frac{1}{r_0}$ (km)	3.5 ± .8	3.9 ± .6	no spheroscale
c	−0.43 ± .08	−0.32 ± .05	−0.18 ± .03
f	0.0 ± .1	−0.01 ± .02	0.00 ± .02
e	−0.4 ± .2	0.17 ± .04	0.04 ± .05
a	0.2 ± .3	0.28 ± .07	0.18 ± .03
$\left(\frac{B}{A}\right)_{\max}$	∞	∞	∞
$\lvert\Delta\theta\rvert_{\max}$ (rad)	1.0 ± .6	0.5 ± .1	0.2 ± .2

in inverse image pixels.) The cloud picture and smoothed Fourier transform for image 1 are shown in Figs. 1 and 2. This image was chosen by colleagues for a study on marine stratocumulus. A "typical" stratocumulus part of a much larger image was isolated for analysis. Since all parameters were previously estimated by a less sophisticated rotating ellipse method[6] (see Pflug 1991), applying the Monte Carlo differential rotation technique was straightforward. For each parameter, two minimizations were performed. In the first succession of minimizations, E_a was calculated over a range of values near the previous estimate for each parameter. In the second set of minimizations, 10 000 points were used for all parameters except e for which 30 000 points were required. In both stages, the parameters were determined in the following order: s, $\log P_l$, U_l ($=\log r_0$), c, f, and e. After the second set of minimizations, quadratics were fit to the E_a versus parameter data to obtain the parameter values. Parameter error estimates were obtained from the concavity of the parabolae fit at the minima.

The data and fitted quadratics for this image are shown in Fig. 3 and the results are listed in Table 1. From this table, we see that $a = 0.2$ for image 1. Since a is real, stratification dominates in this case and the maximum possible rotation is, from Eq. (9), $\lvert\Delta\theta\rvert_{\max} = 1.0$ rad (60 deg). The ellipticity, however, is unlimited.

Image 2: Image 2 is an image of clouds associated with a midlatitude cyclone northeast of Iceland. It is a 512 × 512 pixel *NOAA-9* AVHRR visible image with

FIG. 4. Image 2 (see text for description).

---

[6] This method was an early approximate technique that fit each isoline of $P(\mathbf{k})$ to an ellipse and attempted to estimate $\mathbf{G}$ from the series of ellipses deduced from many isolines.

FIG. 5. Smoothed Fourier transform of image 2.

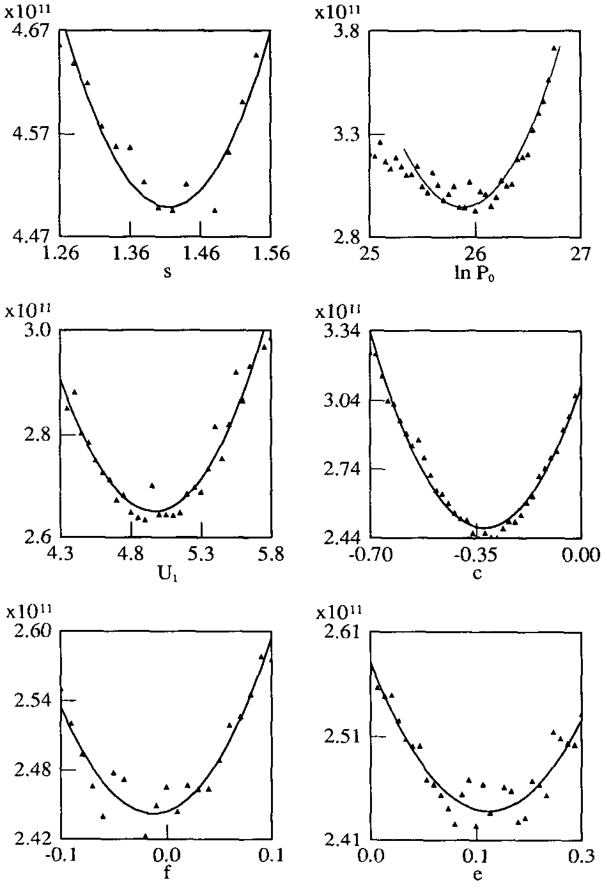

FIG. 6. E_a as a function of the parameters s, $\log P_0$ $s \log r_0 + \log P_1$, $U_1 = \log r_0$, c, f, and e for image 2. The symbols are data points and the solid lines are the fitted quadratics. See Fig. 3 for note about $\log P_0$.

FIG. 7. Image 3 (see text for description).

a resolution of about 1.1 km at nadir. Image 2 is shown in Fig. 4 and its smoothed Fourier transform is shown in Fig. 5. As in the previous case, image 2 was analyzed with the rotating ellipse method (see Pflug 1991) so that good initial estimates of all the parameters were available before starting the Monte Carlo differential rotation analysis. The procedure followed for this image was much the same as that for image 1, except that the number of points in the sum in Eq. (21) was greater as the image is larger. In the second round of mini-

FIG. 8. Smoothed Fourier transform of image 3.

mizations, 100 000 points were required to produce acceptably smooth curves of E_a versus parameter. The results are shown in Fig. 6 and listed in Table 1.

With the values in Table 1, the value of a in this case is 0.28 and $a^2 > 0$. Again, stratification dominates and the maximum total rotation will be $|\Delta\theta|_{\max} = 0.5$ rad (30 deg).

Image 3: This image of a midlatitude cyclone southwest of Iceland and its smoothed Fourier transform are shown in Figs. 7 and 8, respectively. It is a 512 × 512 pixel *NOAA-9* AVHRR visible image with a resolution of about 2.2 km at nadir obtained by sampling every second pixel of a larger 1024 × 1024 pixel image. This image, as compared to images 1 and 2, does not display elliptical isolines in Fourier space. This is to be expected since it has been known since at least Guldberg and Mohn (1877) that cyclones are approximately (scale invariant) log spirals and, hence, are not isotropic at any scale. This is therefore a case in which no spheroscale exists. To define the unit scale, we therefore used the parameterization defined in Eq. (20), which was fit to the second largest level set (see Fig. 12). The number of terms in this series is sufficient to reasonably approximate the shape of the chosen unit ball. The results of this fit are listed in Table 2.

Since the isotropic spectrum for image 3 is already quite straight (Pflug 1991), the spectral slope and intercept (s and $\log P_1$) were estimated from this spectrum and were not reevaluated using the Monte Carlo differential rotation technique. Thus, only c, f, and e were estimated by minimizing Eq. (21), using Eq. (20) and the results in Table 2 to define the unit ball. Two series of minimizations were performed. The initial parameter limits were taken to be -1 and 1 for all three parameters due to the constraints on c and f mentioned earlier and because the isolines in Fig. 8 do not appear to rotate much (larger values of e correspond to more rotation of the Fourier space contours). For all parameters, 100 000 points were included in the sum in Eq. (21) during the second round of minimizations. The E_a versus parameter data and the fitted quadratics for image 3 are shown in Fig. 9 and the parameter estimates are listed in Table 1.

From the results in Table 1, the value of a for this case is 0.18 and $a^2 > 0$. Therefore, stratification dominates and the maximum possible rotation is 0.2 radians (about 11 deg). From Fig. 7, one might have expected that rotation dominates since we naturally associate cyclones with rotation. However, we must not confuse the rotating (spiral) motion of a particle caught in a vortex with the differential rotation of structures as functions of their scales. Indeed, these results show that cyclones are generally not associated with large values of e (or imaginary a); the differential rotation of structures with scale may indeed be small.

TABLE 2. Results of fitting Eq. (20) to the second-largest level set in Fig. 12 to define the unit "ball" for image 3. All parameters are measured in Fourier space pixels.

r_0	108.25 ± .02
a_1	−20.50 ± .02
b_1	−22.74 ± .02
a_2	16.64 ± .02
b_2	−5.70 ± .02

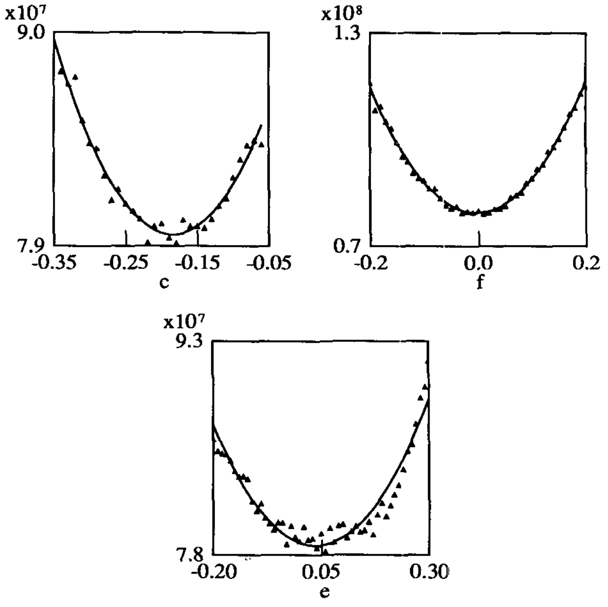

FIG. 9. E_a as a function of the parameters c, f, and e for image 3. The symbols are data points and the solid lines are the fitted quadratics.

Using the results of the Monte Carlo differential rotation analyses of images 1, 2, and 3 (Tables 1 and 2), a series of Fourier space contours for each image was generated by computing $\mathbf{k}_\lambda = \tilde{\mathbf{T}}_\lambda \mathbf{k}_1$ at various scales as indicated above. For comparison, these theoretical contours have been superimposed on the actual Fourier space images and level sets from the Fourier space images in Figs. 10, 11, 12, 13, 14, and 15. As these figures show, the anisotropy appears to have been reasonably well estimated since the fitted contours follow the actual contours quite well.

Clearly, we are at a very early stage in devising empirical tests of scale invariance. We are mostly interested in trying to find GSI systems that are compatible with the observed radiances. Currently, no proper goodness of fit statistics exist, nor will they be trivial to construct. The quality of the fits must, for the moment, be judged mainly by the narrowness of the minima found in parameter space and in the comparison of the theoretical contours with the true Fourier energy surfaces. In the future, anisotropic multifractal simulations with the corresponding generators will be used and the simulations compared with the data. This should provide considerable insight into the preceding results.

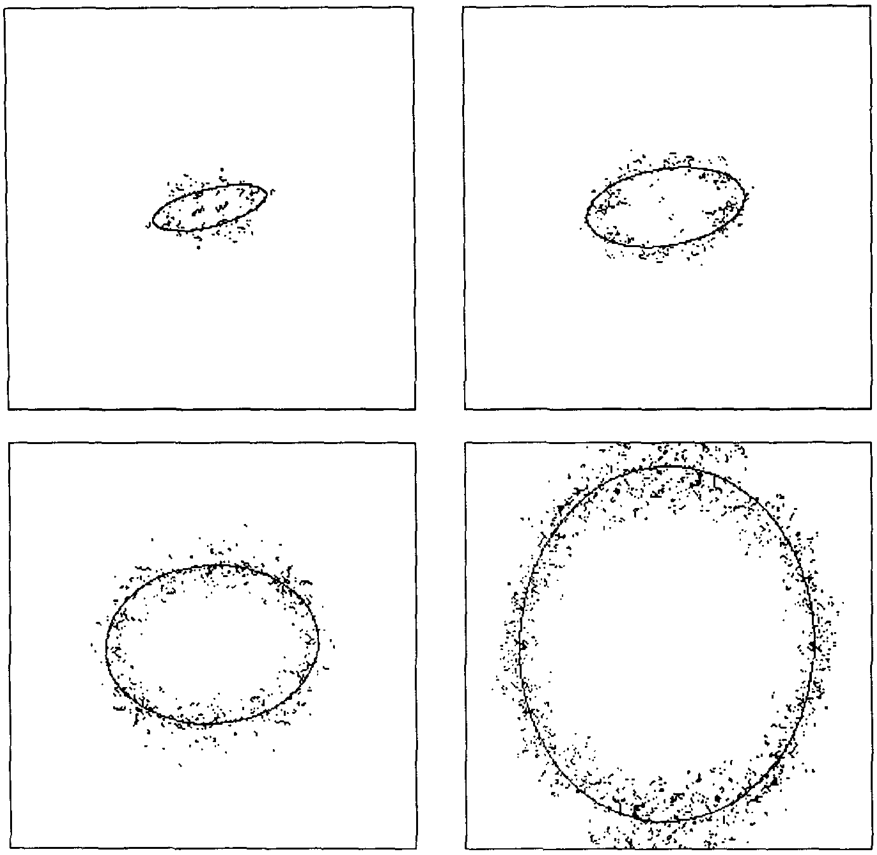

FIG. 10. Level sets (points) and theoretical contours (solid lines) for image 1 at scales ratios: $\lambda = 0.25$, $\lambda = 0.42$, $\lambda = 0.70$, and $\lambda = 1.25$. The theoretical contours were produced using the results in Table 1.

4. Conclusions

The aim of this research has been to develop analysis techniques for studying linear GSI in satellite cloud (and other two-dimensional) images and, using these techniques, to quantify the anisotropy in three different cloud pictures. In so doing, we can determine if linear GSI is a workable approximation for the atmosphere. The full nonlinear GSI, being extremely general, is too difficult to investigate directly. In any case, such knowledge can in principle be obtained by systematically investigating all the tangent spaces (i.e., using linear GSI locally and inferring the global **G** from a series of linearizations). To quantify the anisotropy we have estimated, for each image, the parameters of the generalized scaling operator and the unit ball (the spheroscale where applicable) such that the series of Fourier space contours at all observed scales can be predicted from the estimated generator and unit ball.

Figures 10–15 suggest that the anisotropy has been well estimated for all three images. For all cases, we find that stratification dominates with a maximum possible rotation of 1.0 radians for image 1, 0.5 rad for image 2, and 0.2 rad for image 3. The fact that stratification dominates and rotation is limited for image 3 is interesting because this cyclone image is intuitively associated with rotation. However, such overall rotation is not associated with much differential rotation of structures with scale, and hence, contrary to the intuitive expectation, it only involves small rotation parameters e, and real a (i.e., stratification dominance). We also find spheroscales at 3.5 km in image 1 and 3.9 km in image 2, which fall not too far from 10 km, which is the thickness of the atmosphere based on the falloff in mean pressure. This may in fact be the only way that the thickness of the atmosphere influences the horizontal statistics. There is no spheroscale for image 3; thus, although most of the images examined during the course of this research displayed plausible spheroscales, this is clearly not a requirement for horizontal sections in the atmosphere.

Theoretically, if the radiance field is scaling but anisotropic, the spectra for each image should not be computed isotropically (by integrating around annuli in Fourier space) but rather anisotropically by integrating around the corresponding anisotropic isolines. Indeed, if the energy density isolines ($P(\mathbf{k})$) are very elongated and exhibit substantial rotation as functions

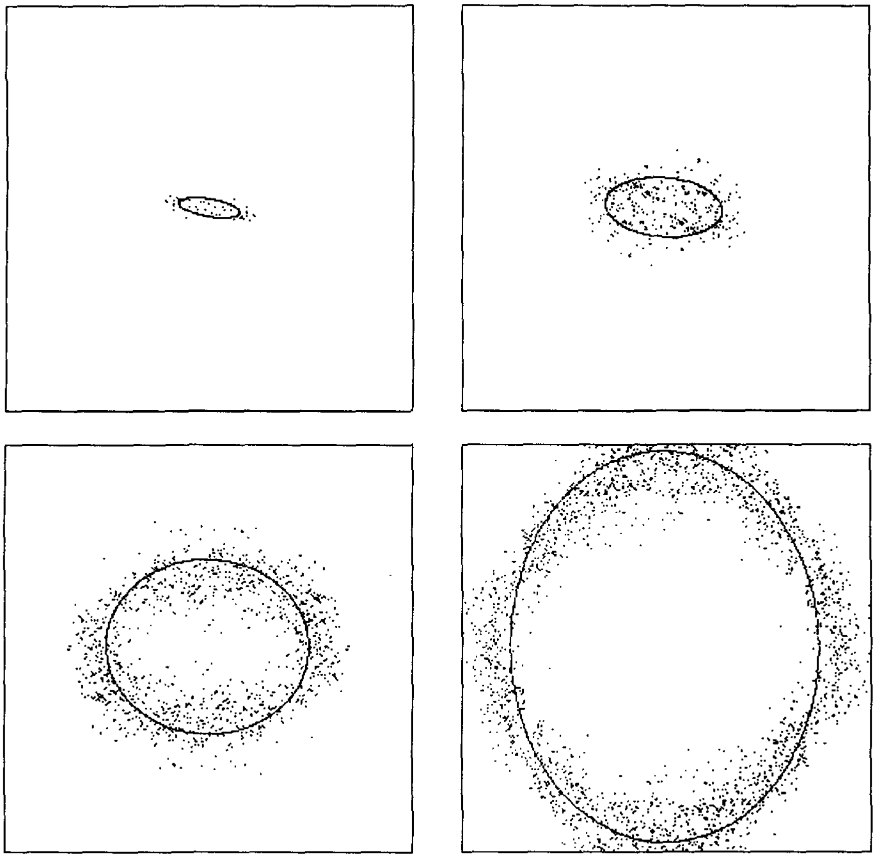

FIG. 11. Level sets (points) and theoretical contours (solid lines) for image 2 at scale ratios: $\lambda = 0.14$, $\lambda = 0.36$, $\lambda = 0.79$, and $\lambda = 1.54$. The theoretical contours were produced using the results in Table 1.

of scale (a imaginary), then the isotropic spectrum will exhibit logarithmically periodic oscillations due to this effect. In the present cases, however, a is real, and the stratification not too extreme (see the contours in Figs. 2, 5, and 8); hence, there is little difference when the spectra are computed anisotropically (Pflug 1991). The angle averaging in Fourier space performed in the computation of the spectrum has washed out most of the manifestations of anisotropy. Our results therefore show how to reconcile reports of power law energy spectra (e.g., Tessier et al. 1993; Lovejoy et al. 1992), with the manifest anisotropy of the cloud radiances.

We have found definite anisotropy and have been able to estimate the corresponding parameters. As expected, we obtain different generators for all three images whose *textures* (meteorological situations) also differ considerably. The robustness of the parameters was confirmed (details in Pflug 1991) for image 1 by comparing two different methods that were biased more toward the small wavenumbers and more toward the large wavenumbers, respectively, both yielding nearly the same **G**. Although many questions remain, our results are consistent with GSI and suggest that linear GSI is a workable approximation. Since the scaling relationship applies to ensemble averages whereas we have analyzed single images, it is quite possible that the remaining discrepancies between the observed and fitted spectra can be readily accounted for; we anticipate a fair amount of statistical scatter. We have, therefore, a reasonably robust, computationally efficient analysis technique. Many more cases must now be analyzed to answer the many outstanding questions, including absolute statistical accuracy of the technique as well as the statistical properties of the linearized **G**.

Since there is now growing evidence that cloud radiances are universal multifractals (Lovejoy and Schertzer 1990a, 1991; Tessier et al. 1993), it is interesting to put the present results in this larger multifractal framework. Recall that **G** was determined from Fourier space (the Fourier transform of the structure function, a second-order moment). In multifractals, there is a one-to-one correspondence between moments and singularities; we have, in fact, characterized the anisotropy of a single order of singularities. A priori, each different order of singularity will have different anisotropy and, hence, a different generator **G**. Al-

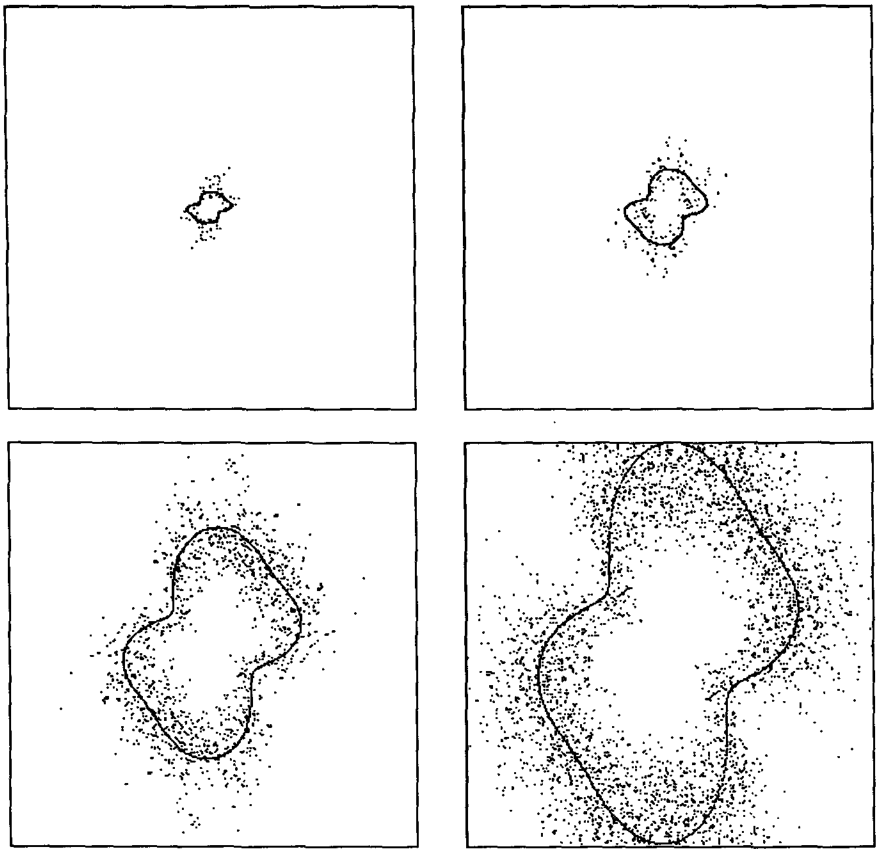

FIG. 12. Level sets (points) and theoretical contours (solid lines) for image 3 at scale ratios: λ = 0.18, λ = 0.38, λ = 1, and λ = 1.58. The theoretical contours were produced using the results in Tables 1 and 2.

FIG. 13. Smoothed Fourier transform of image 1 with theoretical contours determined from the results in Table 1.

FIG. 14. Smoothed Fourier transform of image 2 with theoretical contours determined from the results in Table 1.

FIG. 15. Smoothed Fourier transform of image 3 with theoretical contours determined from the results in Tables 1 and 2.

though preliminary experimentation did not reveal a rapid variation, it will be interesting to systematically estimate **G** for different powers (and hence for different orders of singularity) of the field. All of these results would then benefit by being compared to multifractal simulations. As pointed out in Schertzer and Lovejoy (1991), this work can be extended in a systematic manner by studying the Lie algebra of the coupled generators of the multifractal dynamical cascades and the anisotropy. This may open new perspectives for understanding and analyzing meteorological fields.

APPENDIX A

Linear GSI with Spheroscale

In linear GSI, $\tilde{\mathbf{T}}_\lambda$ is a matrix that depends on four real parameters (c, d, e, f) and is therefore equivalent to a rotation, followed by a stretch, followed by a second rotation. By equating $\tilde{\mathbf{T}}_\lambda$ to this series of rotations and stretches, we obtain the following relations describing the change in shape and orientation of elliptical contours with scale (Pflug 1991)[7]

$$\zeta = 2\left[1 + \left(\frac{e}{a}\right)^2\right]^{1/2} \sinh(au), \qquad (23)$$

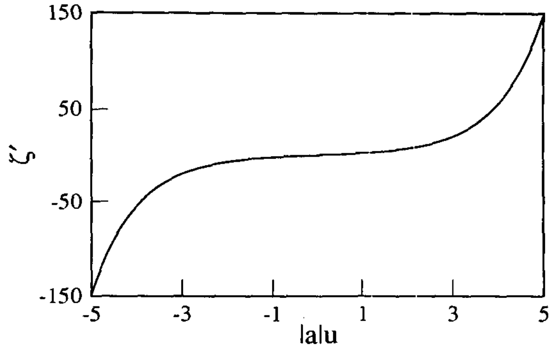

FIG. 16. $\zeta' = \zeta/[1 + (e/a)^2]^{1/2}$ as a function of scale in linear GSI with a spheroscale when $a^2 > 0$ [see Eq. (23)].

$$\epsilon = 2\left[1 + \left(\frac{e}{a}\right)^2\right]^{1/2} \times \sinh(au)\left\langle\left\{\left[1 + \left(\frac{e}{a}\right)^2\right]\sinh^2(au) + 1\right\}^{1/2} + \left[1 + \left(\frac{e}{a}\right)^2\right]^{1/2}\sinh(au)\right\rangle, \qquad (24)$$

$$\theta = \frac{1}{2}\tan^{-1}\left(\frac{f}{c}\right) - \frac{1}{2}\tan^{-1}\left(\frac{e}{a}\tanh(au)\right), \qquad (25)$$

where $u = \log\lambda$, A and B are the ratios of the ellipse semiaxes to the spheroscale radius, $\epsilon = B/A - 1$ is the ellipticity, $\zeta = \sqrt{\epsilon/(\epsilon + 1)} = (B/A)^{1/2} - (A/B)^{1/2}$, and θ is the angle of orientation of the ellipses. At the same time, we find the definition of the scale ratio to be that given in Eq. (11) if the parameter d is set equal to 1 according to the convention in Schertzer and Lovejoy (1987b). The freedom to choose d comes from the arbitrariness to the definition of scale (section 2b). The only restriction is that d be positive. With $d = 1$, $d_{\mathrm{el}} = 2d = 2$ in the horizontal. The behavior determined by Eqs. (23), (24), and (25) is shown in Figs. 16–18, respectively.

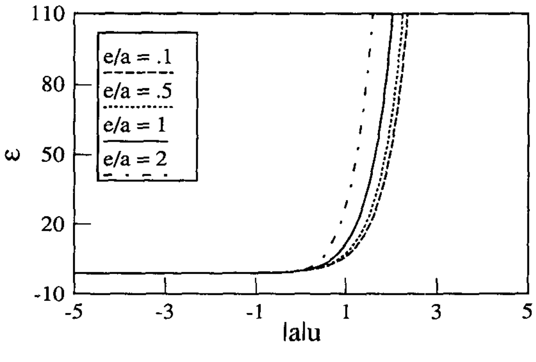

FIG. 17. "Ellipticity" as a function of scale in linear GSI with a spheroscale when $a^2 > 0$ [see Eq. (24)].

---

[7] Recall that we make the simplifying assumption that $\mathbf{T}_\lambda$ is linear and a spheroscale exists in section 2c so contours of $S(\mathbf{x})$ will be elliptical. We use the Fourier space analog (section 2d) to $\mathbf{T}_\lambda$ here since it is more appropriate for our purposes. The results are the same except that λ becomes $1/\lambda$ and e becomes $-e$.

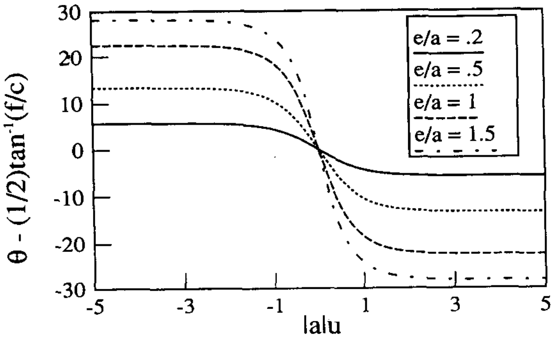

FIG. 18. Angle of orientation (in degrees) as a function of scale in linear GSI with a spheroscale when $a^2 > 0$ [see Eq. (25)]. Only curves with $e > 0$ are shown; if $e < 0$, the curves are flipped about the vertical axis.

In section 2c, two classes of behavior determined by the sign of a^2 are discussed. These results are obtained by examining the ζ, ϵ, and θ equations. When $a^2 > 0$, these equations are as they appear in Eqs. (23), (24), and (25). If $a^2 < 0$, however, these equations can be rewritten in terms of $|a|$ as follows:

$$\zeta = 2\left[\left(\frac{e}{|a|}\right)^2 - 1\right]^{1/2} \sin(|a|u), \qquad (26)$$

$$\epsilon = 2\left[\left(\frac{e}{|a|}\right)^2 - 1\right]^{1/2} \times \sin(|a|u)\left\langle\left\{\left[\left(\frac{e}{|a|}\right)^2 - 1\right]\sin^2(|a|u) + 1\right\}^{1/2} + \left[\left(\frac{e}{|a|}\right)^2 - 1\right]^{1/2}\sin(|a|u)\right\rangle, \qquad (27)$$

$$\theta = \frac{1}{2}\tan^{-1}\left(\frac{f}{c}\right) - \frac{1}{2}\tan^{-1}\left(\frac{e}{|a|}\tan(|a|u)\right). \qquad (28)$$

The behavior determined by Eqs. (26), (27), and (28) is shown in Figs. (19), (20), and (21), respectively.

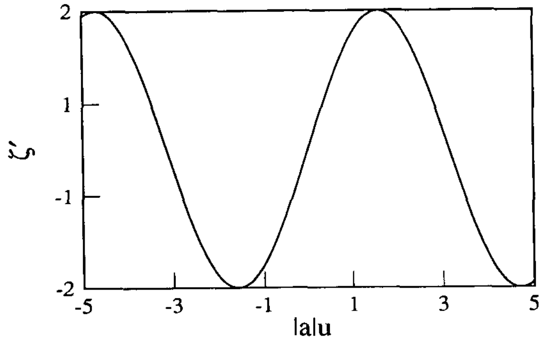

FIG. 19. $\zeta' = \zeta/[(e/|a|)^2 - 1]^{1/2}$ as a function of scale in linear GSI with a spheroscale when $a^2 < 0$ [see Eq. (26)].

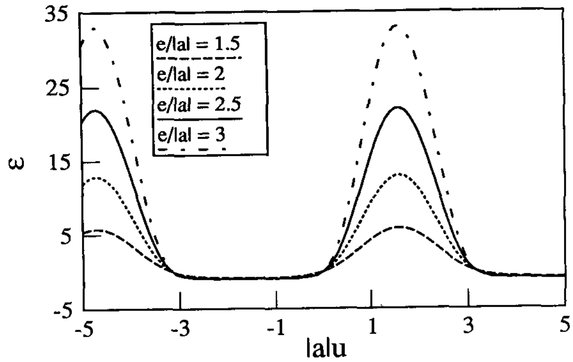

FIG. 20. Ellipticity as a function of scale in linear GSI with a spheroscale when $a^2 < 0$ [see Eq. (27)].

APPENDIX B

Real and Fourier Space GSI

To relate Fourier space and real space scaling, we start with the structure function $S(\mathbf{x})$ of the radiance field $f(\mathbf{x})$ [Eq. (1)]. If $f(\mathbf{x})$ is scale invariant, then the structure function satisfies Eq. (2).

If $F(\mathbf{k})$ is the Fourier transform of $f(\mathbf{x})$, then

$$F(\mathbf{k}) = \left(\frac{1}{2\pi}\right)^D \int f(\mathbf{x}) \exp(-i\mathbf{k}\cdot\mathbf{x}) d\mathbf{x}, \qquad (29)$$

where D is the dimension of space. From the relation (e.g., Monin and Yaglom 1975):

$$P(\mathbf{k}) = \left(\frac{1}{2\pi}\right)^D \int R(\mathbf{x}) \exp(-i\mathbf{k}\cdot\mathbf{x}) d\mathbf{x}, \qquad (30)$$

where $R(\mathbf{x}) = \langle f(\mathbf{x}')f(\mathbf{x} + \mathbf{x}')\rangle = \langle f(0)f(\mathbf{x})\rangle$ and $P(\mathbf{k}) = \langle |F(\mathbf{k})|^2\rangle$, the structure function can be rewritten as

$$S(\mathbf{x}) = 2\int P(\mathbf{k})(1 - \exp(i\mathbf{k}\cdot\mathbf{x}))d\mathbf{k}, \qquad (31)$$

by inverting Eq. (30) and substituting into Eq. (1).

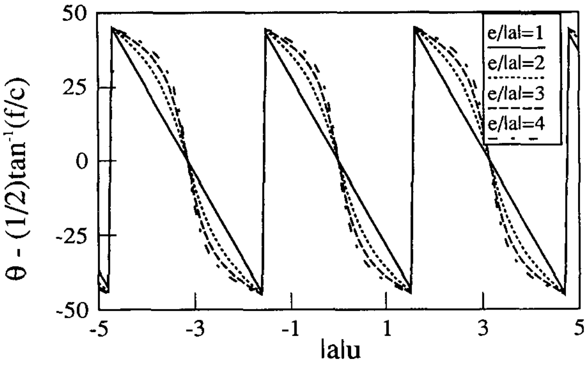

FIG. 21. Angle of orientation, in degrees, as a function of scale in linear GSI with a spheroscale when $a^2 < 0$ [see Eq. (28)]. Only curves with $e > 0$ are shown; if $e < 0$, the curves are flipped on the vertical axis. In this case, $|e/a| \geqslant 1$.

If we let $\mathbf{x} = \mathbf{T}_\lambda \mathbf{x}'$ and $\mathbf{k} = \tilde{\mathbf{T}}_\lambda \mathbf{k}'$, where $\tilde{\mathbf{T}}_\lambda$ is the Fourier space-scaling operator that corresponds to $\mathbf{T}_\lambda$, and define $\tilde{\mathbf{T}}_\lambda = \lambda^{\tilde{\mathbf{G}}}$, then, by requiring invariance of the scalar product under scale changes ($\mathbf{k} \cdot \mathbf{x} = \mathbf{k}' \cdot \mathbf{x}'$), we obtain Eq. (12) defining the Fourier space generator $\tilde{\mathbf{G}}$.

APPENDIX C

Choosing Random Vectors

The m random points in the sum in Eq. (21) are chosen to be uniformly distributed in $\log\lambda$ based on the linear relationship between $\log\lambda$ and $\log P_\lambda$ in Eq. (15). To choose the points in two dimensions, an angle is chosen at the unit scale from a uniform distribution between 0 and 2π and a radius is chosen uniformly in $\log\lambda$ as follows:

$$\log\lambda = ((\log\lambda_{\max})^2 \xi_{N_1})^{1/2} \tag{32}$$

$$\theta = 2\pi\xi_{N_2}, \tag{33}$$

where ξ_{N_1} and ξ_{N_2} are random numbers uniformly distributed between 0 and 1. In effect, we choose a vector with magnitude λ and angle θ. We proceed this way, that is, selecting θ (the angle of $\mathbf{k}_1$) rather than the angle of $\mathbf{k}_\lambda$ since we need to know $\mathbf{k}_1$ in order to compute $\mathbf{k}_\lambda = k(\lambda, \tilde{\mathbf{G}}, \mathbf{k}_1)$ as desired. The maximum scale in Eq. (32) is taken as $\log\lambda_{\max} = \log N/(2)^{1/2} + 1 - \log(\text{area of the unit scale contour}/\pi)^{1/2}$ as explained in Pflug (1991). [Note that (area of the unit scale contour/π)$^{1/2}$ is just r_0. In the case of a spheroscale, see Eq. (20).]

In developing the Monte Carlo differential rotation method, a variation of the technique was tested on one of the images analyzed (image 1) in which the m points in the sum in Eq. (21) were distributed uniformly in λ. There was no significant difference, however, in the results obtained using the two different distributions even though the first distribution is highly concentrated at small wavenumbers while the second is evenly distributed over all wavenumbers. This robustness of the parameter estimates with respect to the distribution of points in the sum is a good indication that the linear approximation to $\tilde{\mathbf{G}}$ holds over the entire range of scales. [For more details and a comparison of the variations, see Pflug (1991)].

Acknowledgments. We thank G. Austin, A. Davis, C. Hooge, D. Lavallée, G. Sarma, F. Schmitt, Y. Tessier, and B. Watson for helpful discussion and comments.

REFERENCES

Adelfang, S. I., 1971: On the relation between wind shears over various intervals. *J. Atmos. Sci.*, **10**, 138.

Atkinson, B. W., 1981: *Mesoscale Atmospheric Circulations.* Academic Press, 257 pp.

Balsley, B. B., and D. A. Carter, 1982: The spectrum of atmospheric velocity fluctuations at 8 km and 86 km. *Geophys. Res. Lett.*, **9**, 465–468.

Bills, B. G., and M. Kobrick, 1985: Venus topography: A harmonic analysis. *J. Geophys. Res.*, **90**, 827–836.

Brown, P. S., and G. D. Robinson, 1979: The variance spectrum of tropospheric winds over eastern Europe. *J. Atmos. Sci.*, **36**, 270–286.

Cahalan, R. F., 1991: Landsat observations of fractal cloud structure. *Scaling, Fractals and Non-linear Variability in Geophysics.* D. Schertzer and S. Lovejoy, Eds., Kluwer, Dordrecht, 281–295.

——, and J. H. Joseph, 1989: Fractal statistics of cloud fields. *Mon. Wea. Rev.*, **117**, 261–272.

Carter, B., and R. N. Henrickson, 1991: A systematic approach to self-similarity in Newtonian space time. *J. Math. Phys.*, **32**, 2580–2599.

Detwiller, A., 1990: Analysis of cloud imagery using box counting. *Int. J. Remote Sens.*, **11**, 887–898.

Endlich, R. M., R. C. Singleton, and J. W. Kaufman, 1969: Spectral analyses of detailed vertical wind speed profiles. *J. Atmos. Sci.*, **26**, 1030–1041.

Gabriel, P., S. Lovejoy, D. Schertzer, and G. L. Austin, 1988: Multifractal analysis of resolution dependence in satellite imagery. *Geophys. Res. Lett.*, **15**, 1373–1376.

Gage, K. S., 1979: Evidence for a $k^{-5/3}$ law inertial range in mesoscale two-dimensional turbulence. *J. Atmos. Sci.*, **36**, 1950–1954.

Grassberger, P., 1983: Generalized dimensions of strange attractors. *Phys. Lett. A*, **97**, 227–230.

Guldberg, C. M., and H. Mohn, 1877: Die Bewegung der Luft in austeigenden Wirbeln. *Wien Met. Zeits.*, **12**, 259–267.

Halsey, T. C., M. H. Jensen, L. P. Kadanoff, I. Procaccia, and B. Shraiman, 1986: Fractal measures and their singularities: The characterization of strange sets. *Phys. Rev. A*, **33**, 1141–1151.

Hentschel, H. G. E., and I. Proccacia, 1983: The infinite number of generalized dimensions of fractals and strange attractors. *Physica*, **8D**, 435–444.

Kraichnan, R. H., 1967: Inertial ranges in two-dimensional turbulence. *Phys. Fluids*, **10**, 1417–1423.

Larchevesque, M., and M. Lesieur, 1981: The application of eddy damped markovian closures to the problem of dispersion of particle pairs. *J. Mech.*, **20**, 113–134.

Lavallée, D., D. Schertzer, S. Lovejoy, and P. Ladoy, 1992: Nonlinear variability of landscape topography: Multifractal analysis and simulation. *Fractals in Geography.* L. De Cola and N. Lam, Eds., Prentice Hall, in press.

Lesieur, M., 1987: *Turbulence in Fluids.* Martinus Nijhoff, 285 pp.

Lilly, D. K., 1983: Mesoscale variability of the atmosphere. *Mesoscale Meteorology-Theories, Observations and Models.* D. K. Lilly and T. Gal-Chen, Eds., D. Reidel, 13–24.

Lovejoy, S., 1982: The area-perimeter relationship for rain and cloud areas. *Science*, **216**, 185–187.

——, and D. Schertzer, 1985: Generalized scale invariance in the atmosphere and fractal models of rain. *Water Resour. Res.*, **21**, 1233–1250.

——, and ——, 1986: Scale invariance, symmetries, fractals and stochastic simulations of atmospheric phenomena. *Bull. Amer. Meteor. Soc.*, **67**, 21–32.

——, and ——, 1990a: Multifractals, universality classes and satellite and radar measurements of cloud and rain fields. *J. Geophys. Res.*, **95**, 2021–2034.

——, and ——, 1990b: Fractals, rain drops and the resolution dependence of rain measurements. *J. Appl. Meteor.*, **29**, 1167–1170.

——, and ——, 1990c: Our multifractal atmosphere: A unique laboratory for nonlinear dynamics. *Phys. Canada*, **46**, 62–71.

——, and ——, 1991: Multifractal analysis techniques and the rain and cloud fields from 10^{-3} to 10^{6} m. *Scaling, Fractals and Non-linear Variability in Geophysics.* D. Schertzer and S. Lovejoy, Eds., Kluwer, 111–144.

——, ——, and A. A. Tsonis, 1987: Functional box-counting and multiple elliptical dimensions in rain. *Science*, **235**, 1036–1038.

——, ——, and K. Pflug, 1992a: Generalized scale invariance and differential rotation in cloud radiances. *Physica A*, **185**, 121–128.

——, ——, P. Silas, Y. Tessier, and D. Lavallée, 1992b: The unified scaling model of the atmospheric dynamics and systematic analysis of scale invariance in cloud radiances. *Ann. Geophys.*, in press.

Monin, A. S., 1972: *Weather Forecasting as a Problem in Physics.* MIT Press, 243 pp.

——, and A. M. Yaglom, 1975: *Statistical Fluid Mechanics Vol. II.* MIT Press, 683 pp.

Nastrom, G. D., and K. S. Gage, 1983: A first look at wavenumber spectra from GASP data. *Tellus,* **35,** 383.

Parisi, G., and U. Frisch, 1985: A multifractal model of intermittency. *Turbulence and Predictability in Geophysical Fluid Dynamics and Climate Dynamics,* M. Ghil, R. Benzi, and G. Parisi, Eds., Elsevier North-Holland, 84–88.

Pentland, A., 1984: Fractal based description of natural scenes. *IEEE Trans. on PAMI,* 661–674.

Pflug, K., 1991: Generalized scale invariance, differential rotation and cloud texture. M. Sc. thesis, Dept. of Physics, McGill University, 94 pp.

——, S. Lovejoy, and D. Schertzer, 1991: Generalized scale invariance, differential rotation and cloud texture. *Nonlinear Dynamics of Structures,* R. Z. Sagdeev, U. Frisch, S. Moiseev, and N. Erokhin, Eds., World Scientific, 71–80.

Pinus, N. Z., 1968: The energy of atmospheric macro-turbulence. *Izv. Acad. Sci. USSR Atmos. Oceanic Phys.,* **4,** 461.

Rhys, F. S., and A. Waldvogel, 1986: Fractal shape of hail clouds. *Phys. Rev. Lett.,* **56,** 784–787.

Schertzer, D., and S. Lovejoy, 1983: Elliptical turbulence in the atmosphere. *Proc. Fourth Symp. on Turbulent Shear Flows.* Karlsrhule, West Germany, 11.1–11.8.

——, and ——, 1984: On the dimension of atmospheric motions. *Turbulence and Chaotic Phenomena in Fluids.* T. Tatsumi, Ed., Elsevier North-Holland, 505–508.

——, and ——, 1985a: The dimension and intermittency of atmospheric dynamics. *Turbulent Shear Flow 4.* B. Launder, Ed., Springer, 7–33.

——, and ——, 1985b: Generalized scale invariance in turbulent phenomena. *P. C. H. Journal,* **6,** 623–635.

——, and ——, 1987a: Singularités anisotropes et divergence de moments en cascades multiplicatifs. *Annales Math. du Que.,* **11,** 139–181.

——, and ——, 1987b: Physical modeling and analysis of rain and clouds by anisotropic scaling multiplicative processes. *J. Geophys. Res.,* **92,** 9693–9714.

——, and ——, 1988: Multifractal simulation and analysis of clouds by multiplicative processes. *Atmos. Res.,* **21,** 337–361.

——, and ——, 1989a: Nonlinear variability in geophysics: Multifractal simulations and analysis. *Fractals: Physical Origin and Consequences.* L. Pietronero, Ed., Plenum, 49–79.

——, and ——, 1989b: Generalized scale invariance and multiplicative processes in the atmosphere. *Pure Appl. Geophys.,* **130,** 57–81.

——, and ——, 1991: Nonlinear geodynamical variability: Multiple singularities, universality and observables. *Scaling, Fractals and Non-linear Variability in Geophysics.* D. Schertzer and S. Lovejoy, Eds., Kluwer, Dordrecht, 41–82.

——, and ——, 1992: Hard and Soft Multifractal processes: *Physica A,* **185,** 187–194.

Schmitt, F., D. Lavallée, D. Schertzer, and S. Lovejoy, 1992: Empirical determination of universal multifractal exponents in turbulent velocity fields. *Phys. Rev. Lett.,* **68,** 305–308.

Tessier, Y., S. Lovejoy, and D. Schertzer, 1993: Universal multifractals: Theory and observations for rain and clouds. *J. Appl. Meteor.,* **32,** 223–250.

Van der Hoven, I., 1957: Power spectrum of horizontal wind speed in the frequency range from 0.0007 to 900 cycles per hour. *J. Meteor.,* **14,** 160–164.

Van Zandt, T. E., 1982: A universal spectrum of buoyancy waves in the atmosphere. *Geophys. Res. Lett.,* **9,** 575–578.

Venig-Meinesz, F. A., 1951: A remarkable feature of the Earth's topography. *Proc. Koninklikjke Nederlandse Akademie Van Wetenschappen. Ser. B Phys. Sci.,* **54,** 212–228.

Vinnichenko, N. K., 1970: The kinetic energy spectrum in the free atmosphere—1 second to 5 years. *Tellus,* **22,** 158–166.

Welch, R. M., K. S. Kuo, B. A. Wielicki, S. K. Sengupta, and L. Parker, 1988: Marine stratocumulus cloud fields off the coast of Southern California observed by Landsat imagery, part I: Structural characteristics. *J. Appl. Meteor.,* **27,** 341–362.

Yano, J.-I., and Y. Takeuchi, 1991: Fractal dimension analysis of horizontal cloud pattern in the intertropical convergence zone. *Scaling, Fractals and Non-linear Variability in Geophysics.* D. Schertzer and S. Lovejoy, Eds., Kluwer, 297–302.